Computational Study of the Structure and Charge-Transfer Parameters in Low-Molecular-Mass P3HT

David L. Cheung,* David P. McMahon, and Alessandro Troisi

*Department of Chemistry and Centre for Scientific Computing, University of Warwick, Coventry CV4 7AL, U.K.*

Using classical molecular dynamics simulations and quantum chemical calculations, the structure and charge-transfer parameters in crystalline poly(3-hexylthiophene) (P3HT) are investigated. The changes in polymer structure with temperature are studied and, by performing DFT calculations on configurations found from MD, the changes in the charge-transfer characteristics are investigated. The system is found to adopt a structure consistent with X-ray diffraction experiments on the so-called type-II polymorph of the poly(3-alkylthiophenes). Upon increasing temperature, a conformational change in the polymer side chains occurs, which is found to lead to increased disorder in the interring torsions, which modulates the charge transfer along the polymer backbone. The intrachain transfer integrals are found to decrease slightly with temperature, while their distribution broadens considerably due to increased thermal motion of the rings. The interchain transfer integrals are found to be appreciable for both nearest and next-nearest neighbor rings. This, taken with the fact that the positions of rings on neighboring chains are strongly correlated, has consequences for the development of more accurate phenomenological charge-transport models, such as variable range hopping models.

Introduction

The investigation of conjugated organic materials for use in electronic devices has a long history, dating back to a few years after the first devices based on inorganic materials.[1] Over the past 20 years, since the demonstration of the first organic light-emitting diodes[2] and thin film transistors, there has been a dramatic rise in interest in these materials. This has been particularly stimulated by the demand for low-cost, large-area semiconducting devices for displays and photovoltaic applications. There are two main classes of organic semiconductors, which are often considered somewhat separately. The first are crystalline molecular semiconductors, which may have exceptionally high charge mobilities, in excess of 10 cm^2 s^{-1} V^{-1},[3,4] but they tend to be difficult to process. The second are polymeric semiconductors, which, due to their self-assembly, are significantly easier to process. Polymer semiconductors, however, typically have lower charge mobilities; the record mobilities are approximately an order of magnitude lower[5] than small molecular organic semiconductors such as pentacene or rubrene.

Organic semiconducting polymers are often characterized by a π-conjugated backbone, and charge transport in semiconducting polymers is sensitive to conformational disorder in the polymer backbone[6,7] and to chemical defects.[8,9] The charge mobility in polymer semiconductors is also strongly dependent on morphology, both at the molecular level and over larger length scales.[10] The motion of charge carriers in these systems, particularly between different chains, is sensitive to the local ordering, and the link between high ordering and charge mobility is well established.[11–13] The need to optimize the chain packing, however, often runs counter to other considerations. The addition of alkyl side chains in order to improve solubility and reduce melting temperatures increases the distance between the polymer chains, which leads to much reduced charge transfer in this
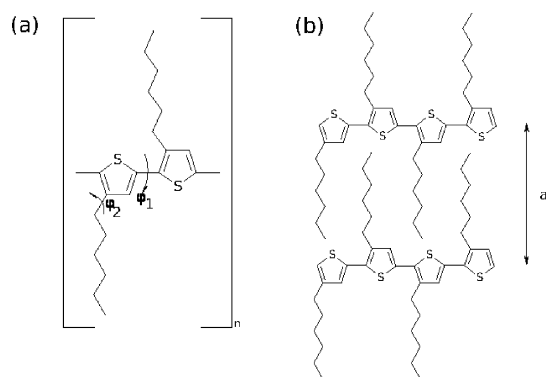
Figure 1. (a) Structure of a regioregular P3HT monomer, showing dihedrals ϕ_1 and ϕ_2. (b) Schematic of the P3HT crystal structure.

direction. Poly(3-alkylthiophene)s [P3ATs] are the archetypal polymer semiconductors, with the hexyl derivative P3HT (Figure 1) having become the de facto reference material for organic electronics. This has been shown to exhibit high charge mobilities, which have been exploited in prototype organic electronic devices.[14–17] P3HT and other semiconducting polymers with side chains form a lamellar structure[18] with two-dimensional conduction within the conjugated sheets, with much reduced charge transfer between sheets.[11] The effect of molecular packing may also be seen by comparing regioregular (RR) and regiorandom (rR) P3HT. RR-P3HT has a charge mobility several orders of magnitude larger than that of rR-P3HT due to its efficient packing and higher interchain overlap.[19,20] On a larger scale, polymer semiconductors often consist of crystalline domains separated by amorphous regions. Molecules in low-molecular-weight (MW) films are able to form well-ordered crystals more easily than those in high-MW films. Despite this higher local ordering in low-MW samples, higher charge mobility has been observed in high-MW P3HT films.[21] This

* To whom correspondence should be addressed. E-mail: david.cheung@warwick.ac.uk.

has been rationalized due to long polymer chains being able to bridge between different crystalline domains.[22]

A number of experimental techniques have been applied to the study of the structure and charge mobility in polymer semiconductors. The morphology has primarily been studied using atomic force microscopy (AFM), which is only able to probe the surface of the sample, and X-ray diffraction (XRD)[23] or scattering.[24] However, X-ray measurements are largely limited to studying the crystalline regions of polymer films, while the amorphous regions are typically large enough to impact charge transport. The charge mobility may be probed by time-of-flight (TOF) measurements,[25] pulse radiolysis time-resolved microwave conductivity (PR-TRMC),[26] space-charge-limited current (SCLC) diodes,[27] or TFTs.[28] Typically however, TOF and PR-TRMC measurements are dominated by the fastest charge carriers, and measurements from SCLC diodes and TFTs may significantly differ from each other.[10]

Because of these limitations in determining both structure and mobility, finding relationships between microscopic structure and charge-transport properties is difficult. Theory and simulation have a particularly important role in modeling, in a consistent way, the heterogeneous experimental data across different materials and morphologies.[29] On the most fundamental level, the electronic structure of these materials may be studied using quantum chemical (QC)[30,31] or plane wave DFT calculations.[32-34] Due to the computational expense of such calculations, these calculations are typically only performed on a small number of predominately low-energy structures or on infinite crystalline systems and therefore may not give a complete picture of the microstrucutre of the materials. In particular, transfer integrals between molecules have been shown to be sensitive to small changes in the molecular environment caused by thermal motion.[35] One use of quantum mechanical calculations has been to derive and parametrize simplified charge-transport models for polymers[36-39] and other organic materials.[40] Charge transport in such systems may be described on a larger scale through the use of phenomenological theories collectively known as variable range hopping (VRH) models.[41] These differ due to assumptions made about, for example, the density of states (e.g Gaussian disorder model),[42] the hopping rates, or correlations between the energies and positions of neighboring sites. These, however, neglect molecular detail and instead use a small number of parameters that can be fit to experimental results. Such methods are particularly useful for the mesoscopic modeling of electric devices.[43]

Due to the direct access to the microscopic scale that molecular simulation affords, it can provide a vital link between the molecular structure and charge mobility in these systems. There is particular interest in combining molecular simulations, which provide information on the structure, with quantum chemical calculations, which can directly study the electronic structure. Such a combitation has been employed in some recent studies of discotic LCs[44-47] and similar systems.[48,49] MD simulations (in combination with quantum chemical calculations) have been combined to study the microstructure and optical properties of amorphous substituted PPV[50] and poly-thiophene[51] and in various phases of substituted oligothiophenes.[52] There has, however, been little previous simulation on the crystalline phases of semiconducting polymers.[53-56] Static lattice and short (<200 ps) molecular dynamics (MD) simulations have been used to study crystalline poly(3-butylthiophene) (P3BT).

Due to the importance of P3HT in materials applications, its microstructure and electronic structure have been the subject of a number of recent studies. Using plane wave DFT calculations, Northrup[57] studied the electronic structure and estimated the charge mobility in polymer seimconductors, including P3HT. More recently, Darling used DFT calculations to study the effect of torsional defects on the intrachain charge-transfer integral,[58,59] and Maillard and Rochefort[60] studied the crystal structure and band structure in P3HT, also using plane wave calculations. In these studies, only a small number of configurations, either low-energy structures or simple deviations from these (e.g., torsional defects), were considered. More recently, a combination of MD and DFT calculations have studied the effect of regioregularity on the charge-transfer behavior in P3HT.[61] This work, however, performed the MD and quantum chemical calculations somewhat in isolation, with the QC calculations being used to study the changes in the charge-transfer parameters for a set of deviations (torsional rotations and changing interchain spacing). Combining MD and QC calculations by using configurations from MD as input for the QC calculations[47] has only recently been performed on P3HT in the amorphous state.[62]

In this paper, we present a study of the microstructure of P3HT using classical MD simulations and quantum chemical calculations. Particular attention is paid to the distribution of dihedral angles in the systems due their importance in charge mobility along the polymer chains. In the next section, the computational methodology used in this work is outlined. Following this, the results, consisting of analysis of thermodynamics, microstructure, dihedral angle distributions, and charge-transfer integrals of the MD and DFT calculations are presented. Finally, conclusions and some avenues for future work are given.

Computational Details

The force field employed in this work was initially used in studies of tetrathiophene.[63,64] Bond stretching and bond angle bending are described by harmonic potentials, with identical equilibrium bond lengths and angles and force constants given by the leading (harmonic) term in the MM3 potentials.[65,66] Cross terms (e.g., stretch−bend, stretch−stretch terms) are neglected. Following refs 64 and 67, nonbonded parameters were taken from the OPLS parameter set,[68] along with the torsional parameters for the alkyl chains. The torsional potential between the thiophene rings was found from high-level ab initio calculations (MP2/aug-cc-pVTZ) on 2-2′-bithiophene.[69] It should be noted that, although bithiophene may not be the most accurate model for the polyalkylthiophenes,[59] a combination of other effects such as crystal packing and the alkyl chains reproduce the experimental dihedral angles, and recent simulations have successfully used torsional potentials parametrized against the bithiophene torsion to model packing of crystalline oligothiophenes[70] and polyalkylthiophene ogilomers.[71] The force field parameters used are presented in Tables S1−S4 in the Supporting Information.

The simulated system consisted of 12 polymer chains, each containing 20 monomers (40 thiophene rings). The initial configuration was the interdigited structure of Prosa et al.,[72] with the distance between the chains initially being 3.8 Å perpendicular to the rings (x direction) and 16 Å parallel to the rings. This crystal structure is expected to be the preferred structure for low-molecular-mass poly(3-alkylthiophenes); for high-molecular-mass P3ATs, a noninterdigited structure is preferred.[73,74]

Simulations were performed using DL_POLY[75] (version 2.18). The equations of motion are integrated using the velocity Verlet integrator, with a time step of 1 fs. Harmonic bonds were constrained using the SHAKE algorithm.[76] The simulations were performed in the constant-*NPT* ensemble, using the Nose−Hoover

Structure and Charge-Transfer in P3HT

J. Phys. Chem. B, Vol. 113, No. 28, 2009 **9395**
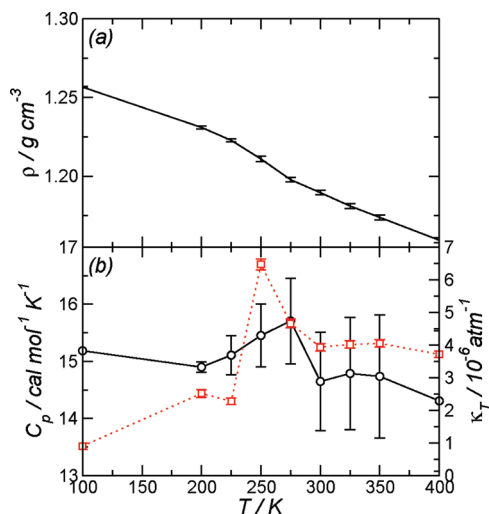
Figure 2. (a) Density (ρ) against T for simulated P3HT. (b) C_p (circles, black) and κ_T (squares, red) against temperature for simulated P3HT.

thermostat and anisotropic barostat[77] with relaxation times of 0.1 and 0.5 ps, respectively. Long-range electrostatics were evaluated using a smooth particle mesh Ewald (SPME) sum,[78] with a convergence parameter of 0.32 Å^{-1} and 16, 16, and 64 wavevectors in the x, y, and z directions, respectively. A cutoff of 9 Å was applied to the short-range van der Waals interactions. Simulations were performed at a range of temperatures (T = 100−400 K). Simulation runs consisted of typically 5−10 ns of equilibration, with statistics gathered over a further 5 ns.

In order to give insight into the charge-transport characteristics, the transfer integrals, between rings on both the same and neighboring chains, were calculated using DFT calculations. The transfer integral is calculated from[35]

$$t_{ij} = \langle \phi_i^0 | \hat{F} | \phi_j^0 \rangle \tag{1}$$

where $\hat{F}$ is the Fock operator for the dimer, and ϕ_i^0 is the unperturbed molecular orbital on each thiophene unit. As P3HT is a hole conductor, the HOMO/HOMO coupling may be expected to be the most important in determining the charge transport; however, as the difference in energy between the HOMO and HOMO-1 orbitals (∼0.046 eV) is small compared to the HOMO/HOMO coupling, the HOMO-1/HOMO-1, HOMO-1/HOMO, and HOMO/HOMO-1 couplings have also been calculated. All of the quantum chemical computations were performed at the B3LYP/6-31G* level of theory.

Results

Thermodynamics and Microstructure. Shown in Figure 2 are the density (ρ), molar heat capacity (C_p^m), and isothermal compressibility (κ_T) determined from simulation. C_p^m and κ_T are found from the usual fluctuation formulas

$$C_p^m = \frac{\langle H^2 \rangle - \langle H \rangle^2}{NRT^2} \tag{2}$$

$$\kappa_T = \frac{\langle V^2 \rangle - \langle V \rangle^2}{k_B T \langle V \rangle} \tag{3}$$

At low (T < 225 K) and high (T > 300 K) temperatures ρ shows a roughly linear decrease with temperature, with a kink between

these two regions. This is accompanied by a peak in C_p and κ_T (Figure 2). Such features are signatures of a structural transition in the system. The precise nature of this will be examined below. The density is higher than the experimental value (ρ = 1.10 g cm^{-3}).[79] However, real samples of P3HT contain both crystalline and amorphous regions; therefore, the experimentally observed density is liable to be somewhat smaller than the crystalline density.

Snapshots showing representative simulation configurations are shown in Figure 3. No major changes from the starting configuration are observed, with the polymer backbones forming two sheets with the alkyl side chains between them.[79] The side chains appear well ordered at T = 100 K (Figure 3a), while at T = 300 K, a degree of disorder may be seen. This will be examined more quantitatively below.

Quantitative information about the microstructure may be found from the radial distribution functions (RDFs). Shown in Figure 4 are partial RDFs, $g_{AB}(r)$. Both the C_1−C_1 and the C_9−C_9 RDFs (the atom types are defined in the Supporting Information) (Figure 4a and d) show very strong peaks at small r (at the C−C bond length) due to bonded neighbors. All of the RDFs have a peak at $r \approx 4$ Å, which corresponds to the separation between monomers on the same chain. At 100 K, this almost coincides with the interchain spacing. As the temperature increases, the interchain spacing increases, and a shoulder develops in this peak. The increase in the interchain spacing with temperature is likely to decrease the charge mobility between neighboring chains. In general, the sharp peaks in the RDFs at low temperatures become diffuse upon increasing temperature, which is most appreciable for the side-chain carbons, C_9 and C_{10} (Figure 4c and d), which results from the increase in disorder in the side chains at higher temperatures.

The interchain spacing depends on temperature, increasing from $r \approx 4.3$ Å at T = 100 K to $r \approx 4.6$ Å at T = 350 K. This relatively large π−π distance and the interdigitation of the side chains suggests that the simulated structure corresponds to the interdigited structure observed by Prosa et al.[72] P3HT also exhibits a noninterdigitated polymorph.[73,74] The influence of the molecular weight on the polymorphism in P3ATs has been studied experimentally, and the interdigited structure was more
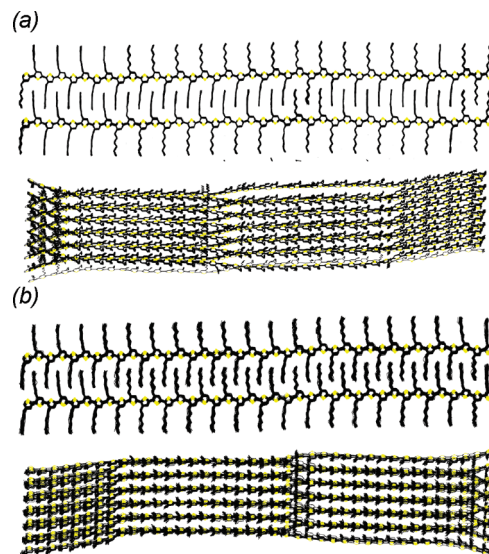
Figure 3. Simulation snapshots at T = (a) 100 and (b) 300 K. Snapshots consist of 10 simulation configurations (separated by 10 ps), and for clarity, hydrogen atoms have been omitted. Generated using the VMD program.[91]
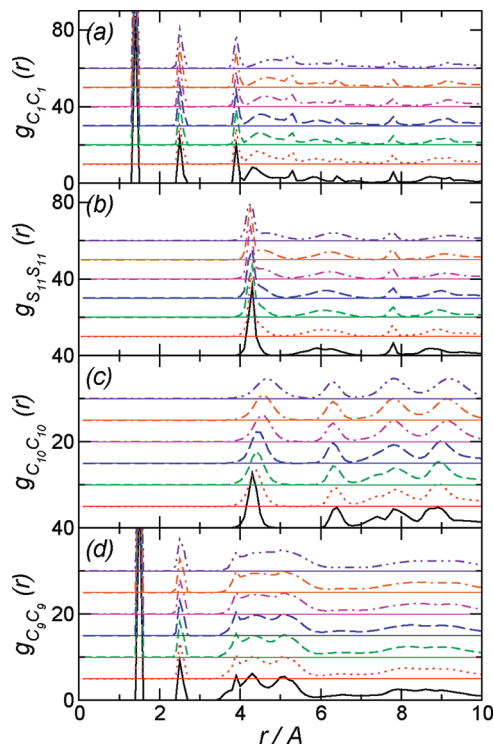
Figure 4. Partial radial distribution functions (a) C_1−C_1, (b) S_{11}−S_{11}, (c) C_{10}−C_{10}, and (d) C_9−C_9. In all cases, $T = 100$ K denoted by solid line (black), $T = 200$ K dotted line (red), $T = 225$ K dashed line (green), $T = 250$ K long dashed line (blue), $T = 275$ K dot−dashed line (magenta), $T = 300$ K dot−double-dashed line (orange), and $T = 350$K double-dot−dashed line (violet). Successive curves are offset by 10 (a and b) or 5 (c and d) units along the y-axis for clarity. Atom types are defined in Figure S-1, Supporting Information.

commonly found for low-molecular-weight samples.[80,81] The polymers studied in this work have a molecular weight around 6700 Da, which is comparable to the molecular weights of low-molecular-mass experimental studies.

Shown in Figure 5 are the dihedral angle distributions for the interring (ϕ_1) and ring-tail (ϕ_2) torsional angles (defined in Figure 1a). Due to the dependence of the coupling between neighboring thiophene rings on their dihedral angle, changes in the distribution of this angle with temperature may play an important role in determining the temperature dependence of intrachain charge transfer.[6,7] While they are expected to have little direct impact on the charge transfer, the side-chain dihedrals affect the molecular packing, which will strongly influence the interchain charge transfer.

At all temperatures studied, the interring torsion (Figure 5a) shows two peaks (of roughly equal height) at about 130 and 230°. This is consistent with the ab initio (gas-phase) torsional potential.[69] It is also in reasonable agreement with X-ray diffraction data, which shows an angle of ∼20−25° between the orientation of the rings and the vertical axis (between chains in neighboring layers). These peaks become more diffuse with temperature due to the increased thermal motion of the rings.

The ring-tail torsion (Figure 5b) varies more dramatically with temperature. At low temperatures, there is a large peak at about $\phi_2 \approx 100°$, corresponding to the side chains pointing along the x-axis. There are a few subsidiary peaks at larger angles, showing that, even at reduced temperatures, there is a degree of conformational disorder in the side chains. Above $T = 250$ K, the distribution changes, with two peaks at $\phi_2 \approx 100$ and 260°. This is consistent with X-ray studies on P3HT, which give an angle of 90° between the ring and chains.[79] The
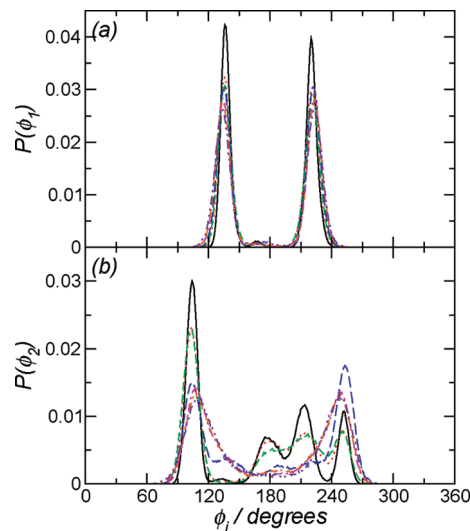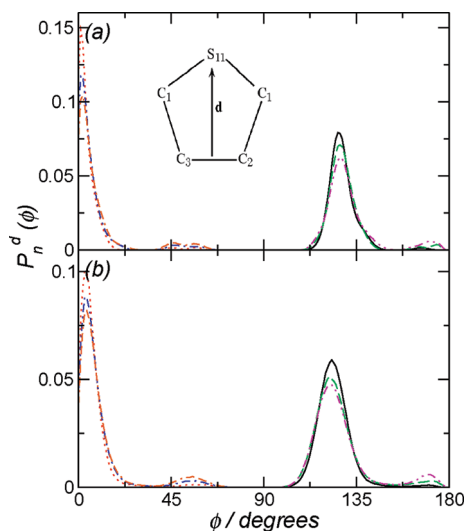

Figure 5. (a) Interring dihedral angle distribution $P(\phi_1)$. Solid line (black) denotes $T = 100$ K, dotted line (red) $T = 200$ K, dashed line (green) $T = 225$ K, long dashed line (blue) $T = 250$ K, dot−dashed line (magenta) $T = 275$ K, dot−double-dashed line (orange) $T = 300$ K, and double-dot−dashed line (violet) $T = 350$ K. (b) Ring-tail dihedral angle distribution. Symbols as in (a).
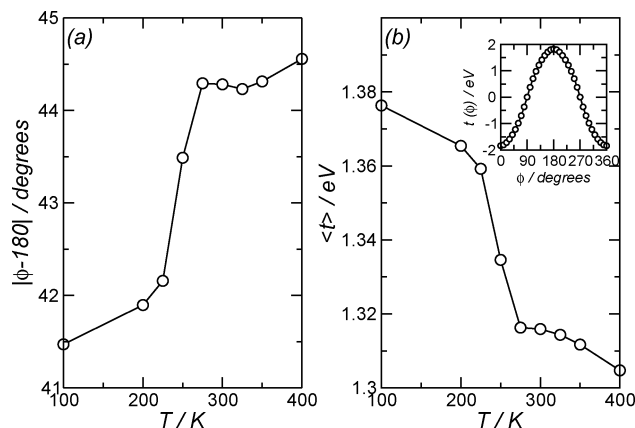
Figure 6. (a) Average deviation from planarity for the backbone dihedral. (b) Average coupling against temperature (calculated from eq 4). Inset shows the variation of coupling, calculated for 2-2′-bithiophene (B3LYP/6-31G*), against the torsional angle.

diffuseness of these peaks, together with the reasonably large probability in the regions between them, indicates that there is a large degree of conformational disorder in the side chains above $T = 250$ K. This transformation is likely to be the cause of the density jump and peaks in C_p^m and κ_T at this temperature (Figure 2).

In common with other alkyl-substituted polymers, the P3ATs show thermochromic behavior (i.e., change in optical properties upon increasing temperature). Experimentally, P3HT displays a broad transition between 270 and 350 K.[82] Studies on other P3ATs have shown that the transition temperature depends on the side-chain length, decreasing from 500 to 270 K when the side-chain length increases from 4 to 20 carbon atoms.[83,84] The thermochromic behavior is attributed to changes in the backbone conformation; large changes in the interring angle lead to decreases in the conjugation length along the polymer backbone, leading to a blue shift in the absorption maximum.[85] The interring dihedral angle distribution (Figure 5a) shows slight variation with increasing temperature, which may be quantified by the average of $|\phi_1 - 180°|$ (Figure 6a). This increases slightly with temperature ($|\phi_1 - 180°| \approx 41.5°$ at 100 K,

Structure and Charge-Transfer in P3HT

J. Phys. Chem. B, Vol. 113, No. 28, 2009 **9397**

Figure 7. Ring probability distributions for T = (a) 100 and (b) 300 K. In both cases, the solid line (black) denotes $n = 1$, dotted line (red) $n = 2$, dashed line (green) $n = 3$, dot−dashed line (blue) $n = 4$, double-dot−dashed line (magenta) $n = 5$, and dot−double-dashed line (orange) $n = 6$.


Figure 8. Time evolution of selected dihedral angles in a single polymer chain at $T = 100$ (left) and 300 K (right). Top shows ϕ_1; bottom shows ϕ_2.

while at 500 K, $|\phi_1 - 180°| \approx 45°$), with a sharp jump at about 250 K. This temperature is approximately the same as the conformational transition in the side chains (Figure 5b). This suggests that due to the close coupling between interring and ring−chain torsions, the side-chain torsions play a large, though indirect, role in the thermochromic behavior.[55] It should be noted that 250 K is lower than the experimentally observed thermochromic transition temperature,[82] and that may be due to differences in molecular weight (the systems studied in ref 82 had an average $M_w \approx 20000$).[86] This change in the interring torsions will also lead to a change in the average interring coupling. This may be estimated from

$$\langle t(T) \rangle = \int \mathrm{d}\phi_1 P(\phi_1, T) t(\phi_1) \qquad (4)$$

where $P(\phi_1, T)$ is the interring dihedral angle probability at a temperature T and $t(\phi_1)$ is the coupling as a function of the interring torsional angle. For this calculation, $t(\phi_1)$ (shown in the inset to Figure 6b) was determined for an isolated 2-2′-bithiophene molecule. The $\langle t(T) \rangle$ decreases with temperature (Figure 6b) due to the wider distribution of dihedral angles. Between $T = 225$ and 275 K, there is sharp drop in $\langle t(T) \rangle$. The behavior of the transfer integrals will be discussed more fully in the next section. While the HOMO/HOMO-1 orbitals of bithiophene are not likely to be a good representation of those of the polymer, the states occupied by the hole can be expressed as a linear combination of monomer orbitals. Therefore, although the monomer-HOMO itself may not be a good state to consider for charge transport, it may still be used to analyze the (intrachain) coupling, which is valid regardless of the localization of the wave function.

Due to the suppression of the backbone dihedral rotations, there may exist long-ranged correlations between the orientations of the thiophene rings. In order to examine this, we calculate the angle between dipoles (defined by the vector joining the midpoint of the C_2-C_3 bond and the S_{11} atom) on different rings on the same polymer chain. The probability distributions $P_i^d(\phi_n)$ (where n denotes separation between the rings) for $T = 100$ and 300 K are shown in Figure 7. A clear alternating structure
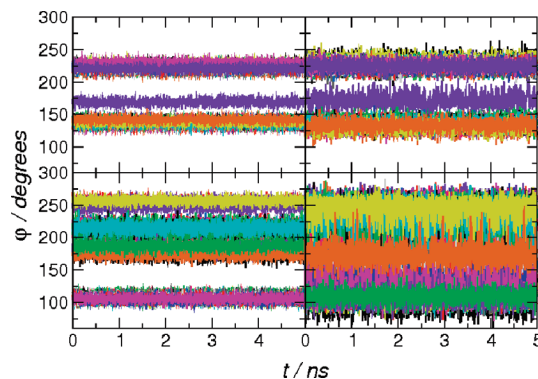
is seen in these, with distributions for odd n being peaked near $\phi = 130°$ and those for even n peaked near $\phi = 0$. This is seen at both $T = 100$ and 300 K, consistent with the lack of a qualitative change in the interring dihedral angle distribution function (Figure 5a). The distributions for even n are sharper than those for odd n, despite these being between rings that are further apart, which may be due to the van der Waals attraction between the side chains on next-nearest-neighboring rings locking them together.

The time evolution of selected dihedral angles for a single chain are shown in Figure 8. No systematic variation is seen in these, with the dihedral angles fluctuating around average values with larger amplitudes at higher temperatures. The interring torsion shows features of both static and dynamic disorder. For both $T = 100$ and 300 K, almost all of the interring torsions fall into two groups around $\phi_1 \approx 130$ and 230°. There is a single dihedral angle (between the seventh and eighth thiophene rings) that lies at an intermediate angle of $\phi_1 \approx 155°$, which arises due to a long-lived defect in the chain. This defect persists for the length of the simulations (over 5 ns) and therefore is static on the simulation time scale and, more importantly, on the typical time scale for charge transport (for a mobility of 0.1 cm^2 s^{-1} V^{-1}, the hole residence time is $10-100$ ps). The distribution for the ring-tail torsion shows more variation between the two temperatures shown. At $T = 100$ K, most of the dihedrals fluctuate close to 100°, with a few lying in the range of $180 \leq \phi_2 \leq 270°$. At $T = 300$ K, the dihedrals are spread across the range $60 \leq \phi_2 \leq 300°$, consistent with the dihedral angle distribution (Figure 5b).

Charge-Transfer Parameters. In order to study the charge-transport characteristics, transfer integrals between rings have been calculated for a selection of MD snapshots. It should be noted that the calculated transfer integral between two rings depends only on their relative positions and orientations (are independent of temperature), and therefore, the differences seen in the average t and its distribution reflect changes in the molecular structure and microstructure at different temperatures. Shown in Figure 9 is the probability distribution of the intrachain transfer integrals (HOMO/HOMO, HOMO/HOMO-1, HOMO-1/HOMO, HOMO-1/HOMO-1) between two neighboring rings. These distributions are all single peaked, with the distribution for the HOMO/HOMO coupling being shifted to higher t relative to the others. The average couplings (presented in Table 1) vary slightly with temperature, with the HOMO/HOMO transfer integral decreasing from 1.18 eV at 100 K to 1.09 eV at 300 K. Apart from the HOMO-1/HOMO-1 coupling, the distribution of t becomes broader at higher temperatures (σ_t increases) due to the increased thermal motion of the rings. In all cases, the
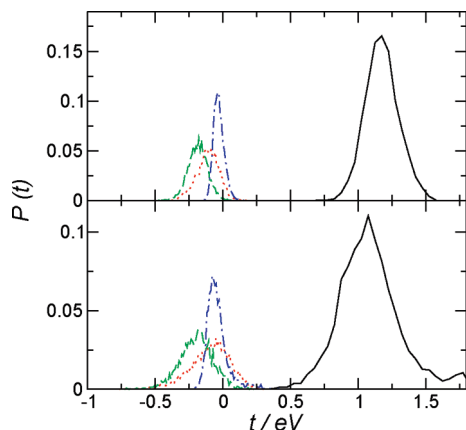
Figure 9. Intrachain transfer integrals t for 100 (top panel) and 300 K (bottom panel). HOMO/HOMO, HOMO/HOMO-1, HOMO-1/HOMO, and HOMO-1/HOMO-1 couplings denoted by solid (black), dotted (red), dashed (green), and dot−dashed (blue) lines, respectively.

TABLE 1: Average Transfer Integrals and Standard Deviations (in eV) at 100 and 300 K

	100 K		300 K	
	$\langle t \rangle$	σ_t	$\langle t \rangle$	σ_t
HOMO/HOMO	1.18	0.12	1.09	0.23
HOMO-1/HOMO	−0.20	0.07	−0.19	0.13
HOMO/HOMO-1	−0.11	0.08	−0.10	0.16
HOMO-1/HOMO-1	−0.03	0.11	−0.04	0.08

distribution of transfer integrals is quite broad, with the standard deviation σ_t being comparable to the difference between the $\langle t \rangle$ at different temperatures. This is similar to the behavior seen in crystalline organic semiconductors[35] and discotic liquid crystals,[44] where charge transfer between molecules is modulated by disorder caused by thermal motion of the molecules. The HOMO-1/HOMO-1 transfer integral is less sensitive to the temperature because the HOMO-1 orbital has a nodal plane passing through the carbon atoms connecting the thiophene rings.

Shown in Figure 10a and b is the distance-dependent average transfer integrals $\bar{t}(r) = \langle t \rangle_r$. These are defined as the average transfer integrals between all rings of separation r, or, more explicitly, in a histogram bin centered around r (note that $\bar{t}(r) = 0$ when there are no rings of a given separation, which leads to the region of $\bar{t}(r) = 0$ at $r \approx 4.8$ Å at 100 K). At both temperatures, the HOMO/HOMO transfer integral decreases, roughly exponentially, with separation due to the decrease in the overlap between the orbitals on each ring. Apart from $r \approx 4.8$ Å, the average HOMO/HOMO transfer integral is smaller at 300 K than that at 100 K; the larger degree of thermal motion at higher temperatures leads to larger deviations in the relative angles between the rings. In contrast to the intrachain coupling, the interchain HOMO-1/HOMO-1 coupling is comparable to the HOMO/HOMO transfer integral. At low separations, the HOMO/HOMO-1 and HOMO-1/HOMO transfer integrals are smaller than the others. Except for the HOMO/HOMO transfer integral, there is a small peak in the transfer intergrals at $r \approx 5$ Å at 100 K and 5.3 Å at 300 K. At both temperatures, the interchain transfer integrals are substantially smaller than the intrachain transfer integral, typically by an order of magnitude, showing that charge transfer is essentially one-dimensional, consistent with experimental studies.

Charge-transport models based on VRH models are characterized by the assumptions made about positional and energetic disorder, the distributions of which are generally parametrized against simulation or developed heuristically. The spatial
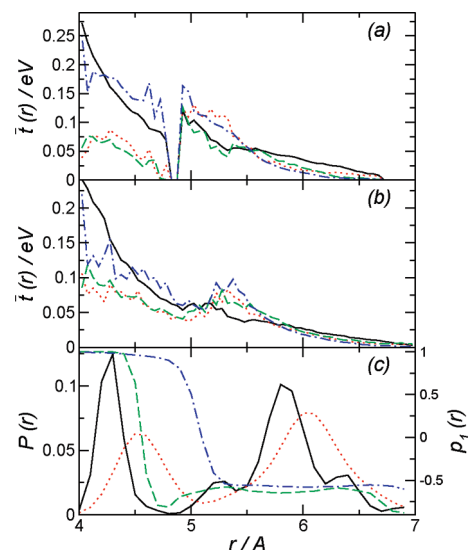
Figure 10. (a) Average interchain transfer integrals at 100 K. HOMO/HOMO, HOMO/HOMO-1, HOMO-1/HOMO, and HOMO-1/HOMO-1 transfer integrals denoted by solid (black), dotted (red), dashed (green), and dot−dashed (blue) lines, respectively. (b) Average interchain transfer integrals at 300 K. Symbols as those in (a). (c) Ring−ring separation probability function $P(r)$ at 100 (solid line, black) and 300 K (dotted line, red) and orientational correlation function $p_1(r)$ at 100 (dashed line, green) and 300 K (dot−dashed line, blue).

TABLE 2: Average Interchain Transfer Integrals for Nearest (t^N) and Next-Nearest (t^{NN}) Neighbor Rings on Adjacent Chains

T/K	coupling	$\langle t^N \rangle$/eV	σ_{t^N}/eV	$\langle t^{NN} \rangle$/eV	$\sigma_{t^{NN}}$/eV
100	HOMO/HOMO	0.16	0.04	0.04	0.02
	HOMO/HOMO-1	0.06	0.05	0.03	0.02
	HOMO-1/HOMO	0.08	0.09	0.03	0.03
	HOMO-1/HOMO-1	0.17	0.08	0.03	0.03
300	HOMO/HOMO	0.09	0.02	0.02	0.01
	HOMO/HOMO-1	0.06	0.06	0.02	0.02
	HOMO-1/HOMO	0.06	0.07	0.02	0.02
	HOMO-1/HOMO-1	0.10	0.09	0.02	0.02

distribution of the rings may be studied though the ring−ring probability distribution $P(r)$ (i.e., the probability of finding two rings of separation r). This is bimodal at both 100 and 300 K (Figure 10b); the first peak, centered at around $r \approx 4.3$ Å at 100 K and 4.6 Å, at 300 K, corresponds to adjacent rings on neighboring chains, while the second peak corresponds to coupling between next-nearest neighbors. This longer-range coupling is often neglected in lattice Monte Carlo simulations[43] (which consider nearest-neighbor couplings) due to the decrease in the transfer integral with distance. The average transfer integrals for nearest- and next-nearest-neighbor chains are presented in Table 2. Due to the increase in interchain spacing, the transfer integrals decrease with temperature. For both temperatures, the nearest-neighbor coupling is approximately four times larger than the next-nearest-neighbor coupling; therefore, the difference between the nearest- and next-nearest-neighbor transfer rates would be, within Marcus−Hush theory,[87,88] approximately an order of magnitude. While this implies that charge hopping between next-nearest-neighbor rings is small, the fact that the difference between the nearest- and next-nearest-neighbor interchain transfer rates is much smaller than those between the intrachain and interchain transfer rates and that each ring has four next-nearest-neighbor rings on adjacent chains, compared to two nearest neighbors, suggests that hopping onto next-nearest neighbors may play an appreciable role in charge

Structure and Charge-Transfer in P3HT

J. Phys. Chem. B, Vol. 113, No. 28, 2009 **9399**

transport. VRH models also typically neglect the mutual arrangement of charge-transport units; however, a strong correlation between ring separation and orientation is observed. This is shown by the orientational correlation function $p_1(r) = \langle \cos \theta \rangle_r$ (Figure 10b), where $\theta = \mathbf{u}_i \cdot \mathbf{u}_j$ is the angle between the dipoles (defined in Figure 7 on two rings of separation r), and this is averaged over all pairs of rings with a separation of r. Nearest-neighbor rings lie close to parallel ($p_1(r) \approx 1$), while for next-nearest-neighbor rings, $p_1(r) \approx -0.6$, corresponding to an angle of approximately 130°. This change in relative orientations leads to the change in the transfer integrals, in particular, the peak in the average HOMO-1/HOMO, HOMO/HOMO-1, and HOMO-1/HOMO-1 transfer integrals, which arise due to a decrease in the separation between the sulfur atoms and the C_2-C_3 bond (on rings on adjacent chains), where the HOMO-1 orbital is largest. The highly inhomogeneous distribution of charge-transfer sites (thiophene units) and the nonmonotonic behavior of the average transfer integrals as a function of separation suggest that the charge carrier motion and charge mobility in P3ATs are more complex than typically assumed in VRH models.

Conclusions

In this paper the microstructure and charge transport parameters have been determined for P3HT, the archetypal microcrystalline, polymer semiconductor, using a combination of atomistic MD simulations and quantum chemical calculations. The main conclusions of the paper are:

• The combination of interdigited side chains and relatively long $\pi-\pi$ spacing (>4.3 Å) is consistent with X-ray diffraction studies on the so-called type-II polymorph of the poly(3-alkylthiophene)s.[72] The existence of this form in simulation is consistent with experimental observations that this form is more commonly found in low-molar-mass samples.[81]

• Upon increasing temperature, a structural transition occurs in the side chain at $T \approx 250$ K, as seen by changes to the dihedral angle distributions and from peaks in the heat capacity and compressibility. Due to the close coupling between the ring-tail and interring torsions, the change in the side-chain conformations also alters the interring torsion with an increase in the average deviation from planarity of the interring torsions. This shows that the side-chain conformations are one of the main driving forces for the thermochromic transitions seen in poly(3-alkylthiophene)s.

• The time evolution of the interring dihedrals shows features of both static and dynamic disorder. Over the length of the simulations, the dihedral angles fluctuate around well-defined average values (no systematic drift is observed). While the dihedral angles largely fall into two groups, with $\phi_1 \approx 130$ and 230°, a small number of the interring dihedrals take different angles. These torsional defects persist thoughout the simulation runs and, on the typical time scale of hole (charge carrier) motion, appear as static disorder.

• The intrachain transfer integrals, determined from DFT calculations, have broad distributions caused by thermal motion of the thiophene rings, with the difference between the average transfer integrals at 100 and 300 K being comparable to or smaller than the width of the distribution. This is similar to the intermolecular transfer integral computed for small-molecule crystalline organic semiconductors, in which charge transfer is modulated by thermal motion.

• The interchain transfer integrals are significantly smaller than the intrachain ones, typically by an order of magnitude. While the interchain transfer integral decreases with distance,
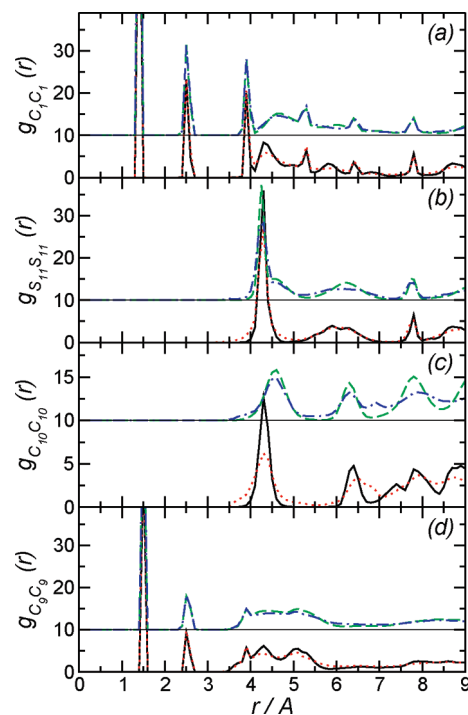
Figure 11. Partial radial distribution functions for (a) C_1-C_1, (b) $S_{11}-S_{11}$, (c) C_9-C_9, and (d) $C_{10}-C_{10}$. Data for 100 K shown by the solid line (12 chains) and dotted line (18 chains), and the 300 K data are shown by the dashed line (12 chains) and dot−dashed line (18 chains).

its decrease is slow enough that there is still an appreciable coupling between the next-nearest-neighbor rings on adjacent chains and that the difference between the coupling between the nearest- and next-nearest-neighbor rings is much smaller than the difference between the intra- and interchain couplings. There is also a strong correlation between the separation between rings and their relative orientations (especially for the transfer integrals involving the HOMO-1 orbitals).

It should be noted that due to the presence of only two layers in the simulation, there may be a strong perdiodicity in the structure. This would most strongly affect the thermodynamics and phase transitions, while the short-range structure will be only weakly affected. To test this, a small number of simulations were performed on three-layer systems (18 chains in total). As demonstrated by the radial distribution functions (Figure 11), only small differences between the structures are seen, with the large system being less ordered than the smaller one. It should also be noted that any additional periodicity imposed by the periodic boundaries will lead to correlations between the layers, whereas the charge-transfer integrals and structural analysis, such as the RDFs (Figure 4), presented in this paper are for chains in the same layer. As charge transport is largely determined by short-ranged interactions (i.e., between adjacent chains in the same layer), any artifacts of the periodic boundaries conditions are likely to only have a small effect on these.

This insight into the microstructure and charge-transport parameters is particularly valuable to improving charge transport (variable range hopping) models. As in previous studies on small-molecule organic semiconductors, liquid crystals, and other polymers, the combination of MD simulations and DFT calculations employed here has been able to calculate the basic parameters that enter into these models, such as the geometry and transfer integrals between rings (charge-transport units). The calculated transfer integrals show that interchain hopping

9400 *J. Phys. Chem. B, Vol. 113, No. 28, 2009*

Cheung et al.

between next-nearest neighbors on adjacent chains typically, neglected in these models, may have an appreciable impact on charge mobility in P3HT. There is also a strong correlation between the separation between rings and their relative orientations, which is contrary to the commonly made assumption that the molecular arrangement (beyond separation) may be neglected.

The extremely slow dynamics in microcrystalline polymers prevents an exhaustive exploration of the conformation space using standard MD. This sampling may be accelerated using techniques such as parallel tempering or replica exchange.[89] The slow dynamics in these systems also makes the investigation of the phase behavior and self-assembly in these systems at an atomistic level intractable. The use of coarse-grained simulations,[90] with potentials derived from atomistic simulations, to investigate the phase behavior and morphology in semiconducting polymers is also currently in progress.

Supporting Information Available: File containing force field parameters. This material is available free of charge via the Internet at http://pubs.acs.org.

References and Notes

(1) Eley, D. D. *Nature* **1948**, *162*, 819–819.

(2) Burroughes, J. H.; Bradley, D. C. C.; Brown, A. R.; Marks, R. N.; MacKay, K.; Friend, R. H.; Burns, P. L.; Holmes, A. B. *Nature* **1990**, *347*, 539–541.

(3) Jurchescu, O. D.; Baas, J.; Palstra, T. T. M. *Appl. Phys. Lett.* **2004**, *84*, 3061–3063.

(4) Podzorov, V.; Menard, E.; Borissov, A.; Kiryukhin, V.; Rogers, J. A.; Gershenson, M. E. *Phys. Rev. Lett.* **2004**, *93*, 086602/1–086602/4.

(5) McCulloch, I.; Heeney, M.; Bailey, C.; Genevicius, K.; MacDonald, I.; Shkunov, M.; Sparrowe, D.; Tierney, S.; Wagner, R.; Zhang, W.; Chabinyc, M. L.; Kline, R. J.; McGehee, M. D.; Tone, M. F. *Nat. Mater.* **2006**, *5*, 328–333.

(6) Salaneck, W. R.; Inganäs, O.; Thémans, B.; Nilsson, J. O.; Sjögren, B.; Österholm, J.-E.; Brédas, J. L.; Svensson, S. *J. Chem. Phys.* **1988**, *89*, 4613–4619.

(7) Choi, J.; Chipara, M.; Xu, B.; Yang, C. S.; Boudin, B.; Dowben, P. A. *Chem. Phys. Lett.* **2001**, *343*, 193–200.

(8) Chambers, D. K.; Karanam, S.; Qi, D.; Selmic, S.; Losovyj, Y. B.; Rosa, L. G.; Dowben, P. A. *Appl. Phys. A* **2005**, *80*, 483–488.

(9) Caruso, A. N.; Feng, D.-Q.; Losovyj, Y. B.; Schulz, D. L.; Balaz, S.; Rosa, L. G.; Sokolov, A.; Doubin, B.; Dowben, P. A. *Phys. Status Solidi B* **2006**, *243*, 1321–1330.

(10) Kline, R. J.; McGehee, M. D. *Polymer Rev.* **2006**, *46*, 27–45.

(11) Sirringhaus, H.; Brown, P. J.; Friend, R. H.; Nielsen, M. M.; Bechgaard, K.; Langeveld-Voss, B. M. W.; Spiering, A. J. H.; Janssen, R. A. J.; Meijer, E. W.; Herwig, P.; de Leeuw, D. M. *Nature* **1999**, *401*, 685–688.

(12) Wang, G.; Swensen, J.; Moses, D.; Heeger, A. J. *J. Appl. Phys.* **2003**, *93*, 6137–6141.

(13) Kline, R. J.; McGehee, M. D.; Toney, M. F. *Nat. Mater.* **2006**, *5*, 222–228.

(14) Sirringhaus, H.; Kawase, T.; Friend, R. H.; Shimoda, T.; Inbasekaran, M.; Wu, W.; Woo, E. P. *Science* **2000**, *290*, 2123–2126.

(15) Huitema, H. E. A. G. H.; Gelinck, G. H.; van der Putten, J. B. P. H.; Kuijk, K. E.; Hart, C. M.; Cantatore,; Herwig, E. P. T.; van Breemen, A. J. J. M.; de Leeuw, D. M. *Nature* **2001**, *414*, 599.

(16) Sandberg, H. G. O.; Frey, G. L.; Shkunov, M. N.; Sirringhaus, H.; Friend, R. H.; Nielson, M. M.; Kumpf, C. *Langmuir* **2002**, *18*, 10176–10182.

(17) Li, G.; Shrotriya, S.; Huang, J.; Yao, Y.; Moriarty, T.; Emery, K.; Yang, Y. *Nat. Mater.* **2005**, *4*, 864–868.

(18) McCullough, R. D. *Adv. Mater.* **1998**, *10*, 93–116.

(19) Bao, Z.; Dodabalapur, A.; Lovinger, A. J. *Appl. Phys. Lett.* **1996**, *69*, 4108–4110.

(20) Österbacka, R.; An, C. P.; Jiang, X. M.; Vardeny, Z. V. *Science* **2000**, *287*, 839–842.

(21) Kline, R. J.; McGehee, M. D.; Kadnikova, E. N.; Liu, J.; Fréchet, J. M. J. *Adv. Mater.* **2003**, *15*, 1519–1522.

(22) Kline, R. J.; McGehee, M. D.; Kadnikova, E. N.; Liu, J.; Frechet, J. M. J.; Toney, M. F. *Macromolecules* **2005**, *38*, 3312–3319.

(23) Winokur, M. J.; Chunwachirasiri, W. *J. Polym. Sci., Part B: Polym. Phys.* **2003**, *41*, 2630–2648.

(24) Aasmundtveit, K.; Samuelsen, E.; Guldstein, M.; Steinsland, C.; Flornes, O.; Fagermo, C.; Seeberg, T.; Pettersson, L.; Inganas, O.; Feidenhans'l, R.; Ferrer, S. *Macromolecules* **2000**, *33*, 3120–3127.

(25) Choulis, S. A.; Nelson, J.; Kim, Y.; Poplavskyy, D.; Kreouzis, T.; Durrant, J. R.; Bradley, D. C. C. *Appl. Phys. Lett.* **2003**, *83*, 3812–3814.

(26) Hoofman, R. J. O. M.; de Hass, M. P.; Siebbles, L. D. A.; Warman, J. M. *Nature* **1998**, *392*, 54–56.

(27) Bozano, L.; Carter, S. A.; Scott, J. C.; Malliaras, G. G.; Brock, P. J. *Appl. Phys. Lett.* **1999**, *74*, 1132–1134.

(28) Tanase, C.; Meijer, E. J.; Blom, P. W. M.; de Leeuw, D. M. *Phys. Rev. Lett.* **2003**, *91*, 216601/1–4.

(29) Cheung, D. L.; Troisi, A. *Phys. Chem. Chem. Phys.* **2008**, *10*, 5941–5952.

(30) Moro, G.; Scalmani, G.; Cosentine, U.; Pitea, D. *Synth. Met.* **2000**, *108*, 165–172.

(31) Zade, S. S.; Bendikov, M. *Chemistry* **2007**, *13*, 3688–3700.

(32) Vogl, P.; Campbell, D. K. *Phys. Rev. Lett.* **1989**, *62*, 2012–2015.

(33) Vogl, P.; Campbell, D. K. *Phys. Rev. B* **1990**, *41*, 12797–12817.

(34) Zheng, G.; Clark, S. J.; Brand, S.; Abram, R. A. *J. Phys. Condens. Matter* **2004**, *16*, 8609–8620.

(35) Troisi, A.; Orlandi, G. *J. Phys. Chem. A* **2006**, *110*, 4065–4070.

(36) Grozema, F. C.; van Duijnen, P. T.; Berlin, Y. A.; Ratner, M. A.; Siebbles, L. D. A. *J. Phys. Chem. B* **2002**, *106*, 7791–7795.

(37) Prins, P.; Grozema, F. C.; Siebbles, L. D. A. *J. Phys. Chem. B* **2006**, *110*, 14659–14666.

(38) Prins, P.; Grozema, F. C.; Siebbles, L. D. A. *Mol. Simul.* **2006**, *32*, 695–705.

(39) Grozema, F. C.; Siebbles, L. D. A. *Int. Rev. Phys. Chem.* **2008**, *27*, 87–138.

(40) Troisi, A.; Orlandi, G. *Phys. Rev. Lett.* **2006**, *96*, 086601/1–4.

(41) *Charge transport in disordered solids with applications in electronics*; Baranovski, S., Ed.; John Wiley and Sons Ltd: Chichester, U.K., 2006.

(42) Bässler, H. *Phys. Status Solidi B* **1993**, *175*, 15–56.

(43) Athanasopoulos, S.; Kirkpatrick, J.; Martínez, D.; Frost, J. M.; Foden, C. M.; Walker, A. B.; Nelson, J. *Nano Lett.* **2007**, *7*, 1785–1788.

(44) Kirkpatrick, J.; Marcon, V.; Nelson, J.; Kremer, K.; Andrienko, D. *Phys. Rev. Lett.* **2007**, *98*, 227402/1–227402/4.

(45) Andrienko, D.; Kirkpatrick, J.; Marcon, V.; Nelson, J.; Kremer, K. *Phys Status Solidi B* **2008**, *245*, 830–834.

(46) Marcon, V.; Kirkpatrick, J.; Pisula, W.; Andrienko, D. *Phys. Status Solidi B* **2008**, *245*, 820–824.

(47) Kirkpartrick, J.; Marcon, V.; Nelson, J.; Kremer, K.; Andrienko, D. *Phys. Status Solidi B* **2008**, *245*, 835–838.

(48) Kwiatkowski, J. J.; Nelson, J.; Li, H.; Bredas, J. L.; Wenzel, W.; Lennartz, C. *Phys. Chem. Chem. Phys.* **2008**, *10*, 1852–1858.

(49) Rühle, V.; Kirkpatrick, J.; Kremer, K.; Andrienko, D. *Phys. Status Solidi B* **2008**, *245*, 844–848.

(50) Yang, H.-C.; Hua, C.-Y.; Kuo, M.-Y.; Huang, Q.; Chen, C.-L. *ChemPhysChem* **2004**, *5*, 373–381.

(51) Curćo, D.; Alemán, C. *J. Comput. Chem.* **2007**, *28*, 1743–1749.

(52) Marcon, V.; van der Vegt, N.; Wegner, G.; Raos, G. *J. Phys. Chem. B* **2006**, *110*, 5253–5261.

(53) Corish, J.; Feeley, D. E.; Morton-Blake, D. A.; Bénière, F.; Marchetti, M. *J. Phys. Chem. B* **1997**, *101*, 10075–10085.

(54) Xie, H.; Corish, J.; Morton-Blake, D. A. *Synth. Met.* **2000**, *113*, 65–72.

(55) Xie, H.; O'Dwyer, S.; Corish, J.; Morton-Blake, D. A. *Synth. Met.* **2001**, *122*, 287–296.

(56) O'Dwyer, S.; Xie, H.; Corish, J.; Morton-Blake, D. A. *J. Phys.: Condens. Matter* **2001**, *13*, 2395–2410.

(57) Northrup, J. E. *Phys. Rev. B* **2007**, *76*, 245202/1–245202/6.

(58) Darling, S. B. *J. Phys. Chem. B* **2008**, *112*, 8891–8895.

(59) Darling, S. B.; Sternberg, M. *J. Phys. Chem. B* **2009**, *113*, 6215–6218.

(60) Maillard, A.; Rochefort, A. *Phys. Rev. B* **2009**, *79*, 115207/1–7.

(61) Lan, Y.-K.; Huag, C.-I. *J. Phys. Chem. B* **2008**, *112*, 14857–14862.

(62) Vukmirović, N.; Wang, L.-W. *J. Phys. Chem. B* **2009**, *113*, 409–415.

(63) Marcon, V.; Raos, G. *J. Am. Chem. Soc.* **2006**, *128*, 1408–1409.

(64) Marcon, V.; Raos, G.; Campione, M.; Sassella, A. *Cryst. Growth Des.* **2006**, *6*, 1826–1832.

(65) Allinger, N. L.; Yuh, Y. H.; Lii, J.-H. *J. Am. Chem. Soc.* **1989**, *111*, 8551–8566.

(66) Yang, L.; Allinger, N. L. *J. Molec. Struct.: THEOCHEM* **1996**, *370*, 71–83.

(67) Gus'kova, O. A.; Mena-Osterlitz, E.; Schillinger, E.; Khalatur, P. G.; Bäuerle, P.; Khokhlov, A. R. *J. Phys. Chem. C* **2007**, *111*, 7165–7174.

(68) Jorgensen, W. L.; Maxwell, D. S.; TiradoRives, J. *J. Am. Chem. Soc.* **1996**, *118*, 11225–11236.

Structure and Charge-Transfer in P3HT

J. Phys. Chem. B, Vol. 113, No. 28, 2009 **9401**

(69) Marcon, V.; Raos, G. *J. Phys. Chem. B* **2004**, *108*, 18053–18064.

(70) Maron, V.; Raos, G.; Allegra, G. *Macrom. Theory Simul.* **2004**, *13*, 497–505.

(71) Arosio, P.; Moreno, M.; Famulari, A.; Roas, G.; Catellani, M.; Meille, S. V. *Chem. Mater.* **2009**, *21*, 78–87.

(72) Prosa, T. J.; Winokur, M. J.; McCullough, R. D. *Macromolecules* **1996**, *29*, 3654–3656.

(73) Yamamoto, T.; Komarudin, D.; Arai, M.; Lee, B.-L.; Suganuma, H.; Asakawa, N.; Inoue, Y.; Kubota, K.; Sasaki, S.; Fukuda, T.; Matsuda, H. *J. Am. Chem. Soc.* **1998**, *120*, 2047–2058.

(74) Kline, R. J.; DeLongchamp, D. M.; Fischer, D. A.; Lin, E. C.; Richter, L. J.; Chabinyc, M. L.; Toney, M. F.; Heeney, M.; McCulloch, I. *Macromolecules* **2007**, *40*, 7960–7965.

(75) Smith, W.; Forester, T. R. *J. Mol. Graphics* **1996**, *14*, 136–141.

(76) Ryckaert, J.-P.; Ciccotti, G.; Berendsen, H. J. C. *J. Comput. Phys.* **1977**, *23*, 327–341.

(77) Melchionna, S.; Ciccotti, G.; Holian, B. L. *Mol. Phys.* **1993**, *78*, 533–544.

(78) Essmann, U.; Perera, L.; Berkowitz, M. L.; Darden, T.; Lee, H.; Pedersen, L. G. *J. Chem. Phys.* **1995**, *103*, 8577–8593.

(79) Prosa, T. J.; Winokur, M. J.; Moulton, J.; Smith, P.; Heeger, A. J. *Macromolecules* **1992**, *25*, 4364–4372.

(80) Meille, S. V.; Romita, V.; Caronna, T.; Lovinger, A. J.; Catellani, M.; Belobrzeckaja, L. *Macromolecules* **1997**, *30*, 7898–7905.

(81) Joshi, S.; Grigorian, S.; Pietsch, U. *Phys. Status Solidi A* **2008**, *205*, 488–496.

(82) Winkour, M. J.; Spiegel, D.; Kim, Y.; Hotta, S.; Heeger, A. J. *Synth. Met.* **1989**, *28*, C414–C426.

(83) Tashiro, K.; Ono, K.; Mingawa, Y.; Kobayashi, M.; Kawai, T.; Yoshino, K. *J. Polym. Sci., Part B: Polym. Phys.* **1991**, *29*, 1223–1233.

(84) Tachibana, H.; Hosaka, N.; Tokura, Y. *Macromolecules* **2001**, *34*, 1823–1827.

(85) Leclerc, M.; Fréchette, M.; Bergeron, J.-Y.; Ranger, M.; Lévesque, I.; Faïd, K. *Macromol. Chem. Phys.* **1996**, *197*, 2077–2087.

(86) Hotta, S.; Rughooputh, S. D. D. V.; Heeger, A. J.; Wudl, F. *Macromolecules* **1987**, *20*, 212–215.

(87) Marcus, R. A. *Rev. Mod. Phys.* **1993**, *65*, 599–610.

(88) Bredás, J. L.; Calbert, J. P.; da Silva Filho, D. A.; Cornil, J. *Proc. Natl. Acad. Sci. U.S.A.* **2002**, *99*, 5804–5809.

(89) Earl, D. J.; Deem, M. W. *Phys. Chem. Chem. Phys.* **2005**, *7*, 3910–3916.

(90) Cheung, D. L.; Troisi, A. *Phys. Chem. Chem. Phys.* **2009**, *11*, 2105–2112.

(91) Humphery, W.; Dalke, A.; Schultern, K. *J. Mol. Graphics* **1996**, *14*, 33–38.